Supplement of Atmos. Chem. Phys., 26, 8367–8385, 2026
https://doi.org/10.5194/acp-26-8367-2026-supplement

Atmospheric Chemistry and Physics
Open Access
EGU

Supplement of

Impacts of entrainment on secondary ice production in deep convective clouds

Bowen Z. Portman et al.

Correspondence to: Paul J. Connolly (paul.connolly@manchester.ac.uk)

S1 Secondary ice parametrisations

Four SIP mechanisms are represented in the model, following the same parametrisations as those used by James et al. (2023). These include rime splintering (RS), collisional breakup between ice particles (CB), spherical freezing fragmentation of drops (M1), and fragmentation between supercooled droplets and more massive ice particles (M2).

S1.1 Rime splintering (RS)

We first describe the RS parametrisation in the BMM. In this model, splinter production is determined by the riming rate calculated using the SCE with the exponential flux method of Bott (1998), and occurs only within the temperature range of -2.5 to $-7.5\,^{\circ}\mathrm{C}$, with a maximum near $-5\,^{\circ}\mathrm{C}$, consistent with the laboratory findings of Hallett and Mossop (1974). The newly generated splinters are then introduced into the smallest ice particle bin, after which they continue to evolve through the other cold microphysical processes. The splinter production rate is represented using a modified formulation based on Reisner et al. (1998), given by:

$$\frac{dN_{\mathrm{RS}}}{dt} = 350 \times 10^{6} \left(\frac{dm_r}{dt} \right) f_{\mathrm{RS}}(T) \tag{S1}$$

where $\frac{dN_{\mathrm{RS}}}{dt}$ is the splinter production rate due to RS, $\frac{dm_r}{dt}$ is the riming rate, and $f_{\mathrm{RS}}(T)$ is the temperature-dependent efficiency function, which has a maximum of unity at $T = -5^{\circ}\mathrm{C}$ and is zero for $T < -2.5^{\circ}\mathrm{C}$ and $T > -7.5^{\circ}\mathrm{C}$.

S1.2 Ice–Ice collisional breakup (CB)

The CB parametrisation in the BMM follows Phillips et al. (2017), in which the number of fragments produced per collision is parameterised as a function of collisional kinetic energy and the characteristics of the colliding ice particles. The fragment number is given by

$$N_{CB} = \alpha A \left(1 - \exp\left\{ - \left[\frac{C K_{0(CB)}}{\alpha A} \right]^{\gamma} \right\} \right) \tag{S2}$$

where $\alpha = \pi D^2$ is the equivalent spherical surface area of the smaller colliding particle, and A, C, and γ are empirical parameters associated with the contact asperity density, fragility, and riming intensity, respectively. $K_{0(CB)}$ is the collisional kinetic energy calculated by:

$$K_{0(CB)} = \frac{1}{2} \left(\frac{m_1 m_2}{m_1 + m_2} \right) (v_1 - v_2)^2 \tag{S3}$$

where m_1 and m_2 are the mass of the colliding ice particles, and v_1 and v_2 are their fall speeds.

Following Phillips et al. (2017), three collision categories are considered: graupel or hail with graupel or hail, hail with hail, and snow or ice crystals (dendritic or spatial planar) with any ice particle. The parameters A, C, and γ depend on the collision category, as summarised in Table 1 of Phillips et al. (2017). In the BMM, the colliding ice particles are classified using the modelled density, rime mass, and aspect ratio, and the corresponding criteria are listed in Table S1, following James et al. (2023).

S1.3 Freezing Fragmentation of drops: Mode 1 (M1)

The M1 parametrisation is based on Phillips et al. (2018), who summarised laboratory data on the freezing fragmentation of drops. When fragmentation occurs, the fragments are separated into two size classes: small fragments, which are more numerous and smaller, and large fragments, which are fewer and larger. Phillips et al. (2018) showed that M1 is most efficient

Table S1. Criteria used in the BMM to classify colliding ice particles for the CB parametrisation. These criteria are used in conjunction with Table 1 of Phillips et al. (2017) to determine the appropriate parameter values in Eq. S2. Reproduced from James et al. (2023).

Collision type	D_s (m)	R_{FS}	R_{FL}	ρ_L (kg m^{-3})	Φ_S
Graupel with graupel or hail	5×10^{-4} to 5×10^{-3}	$0.5 \leq R_{FS} < 0.9$	≥ 0.5	n/a	n/a
Hail with hail	n/a	≥ 0.9	> 0.9	n/a	n/a
Dendrites with any ice particle	5×10^{-4} to 5×10^{-3}	< 0.5	n/a	< 400	< 1
Spatial planar with any ice particle	5×10^{-4} to 5×10^{-3}	< 0.5	n/a	≥ 400	< 1

near $-15\,^{\circ}$C. The parametrisations for the total number of fragments (N_{M1T}) and the number of large fragments (N_{M1L}) are given below:

$$N_{M1T} = F(D)\Omega(T)\left[\frac{\zeta\eta^2}{(T-T_0)^2+\eta^2} + \beta T\right] \tag{S4}$$

$$N_{M1L} = min\left\{F(D)\Omega(T)\left[\frac{\zeta_B\eta_B^2}{(T-T_{B0})^2+\eta_B^2}\right], N_T\right\} \tag{S5}$$

where ζ, η, β, ζ_B, η_B, T_0, T_{B0} are parameters taken from Phillips et al. (2018) which were derived from fitting Lorentzians to the laboratory data. $F(D)$ and $\Omega(T)$ are interpolation functions for the onset of fragmentation, and T is the freezing temperature of the drop.

S1.4 Freezing Fragmentation of drops: Mode 2 (M2)

The M2 parametrisation follows Phillips et al. (2018), in which fragmentation is assumed to be controlled by the ratio of collision kinetic energy, K_0, to the initial surface energy, here denoted by the dimensionless energy, *DE*. M2 fragmentation occurs only when the drop diameter exceeds 0.15 mm and the drop is less massive than the colliding ice particle. The quantities K_0 and *DE* are calculated as follows:

$$K_0 = \frac{1}{2}\left(\frac{m_d m_i}{m_d + m_i}\right)(v_d - v_i)^2 \tag{S6}$$

$$DE = \frac{K_0}{\gamma_l \pi D_d^2} \tag{S7}$$

where m_d and m_i are the mass of the drop and ice respectively, v_d and v_i are the velocity of the drop and ice particle respectively, D_d is the diameter of the drop and γ_l is the surface tension of liquid water which is set as a constant of 0.073 J m^{-2}.

The number of fragments generated per drop accreted through M2, N_{M2}, is then calculated as:

$$N_{M2} = 3\Phi(T) \times [1 - f(T)] \times \max(DE - DE_{crit}, 0) \tag{S8}$$

where Φ is the probability that a splash droplet contains ice, $f(T)$ is the temperature-dependent frozen mass fraction of a drop by the end of stage 1 freezing, defined as $f(T) = -c_w T/L_f$, and DE_{crit} is the critical value of DE for onset of splashing ($\sim$0.2). The value of Φ is set to 0.3 following James et al. (2021).

S2 Representation of heterogeneous ice nucleation

Primary ice formation by heterogeneous nucleation is represented using the INP parametrisation derived from DCMEX observations of Daily et al. (2025). For comparison, the widely used INP parametrisation of DeMott et al. (2010) is also considered.

S2.1 Reference INP parametrisation (DeMott et al., 2010)

The INP parametrisation of DeMott et al. (2010) provides an empirical relationship for the number concentration of ice-nucleating particles as a function of temperature and the number concentration of aerosol particles with diameters larger than $0.5\,\mu\mathrm{m}$. The parametrisation is given by

$$N_{\mathrm{INP}}(T_k) = a\,(273.16 - T_k)^{b}\,(n_{a,>0.5\mu m})^{\,c(273.16-T_k)+d}, \tag{S9}$$

where T_k is temperature in K, $n_{a,>0.5\mu m}$ is the number concentration of aerosol particles with diameters larger than $0.5\,\mu\mathrm{m}$, and the empirical coefficients are $a = 5.94 \times 10^{-5}$, $b = 3.33$, $c = 0.0264$, and $d = 0.0033$.

S2.2 DCMEX-based INP parametrisation (Daily et al., 2025)

The second is a temperature-dependent INP parametrisation developed by Daily et al. (2025) based on DCMEX observations, which uses a two-part fit to the observed INP data. It is based on airborne filter INP measurements, followed by droplet freezing measurements. The parametrisation is given by

$$N_{\mathrm{INP}} = A_{\mathrm{dust}} F_{\mathrm{Kfsp}} n_s(T) + a \exp[b\,(T_{\max} - T)^{c}], \tag{S10}$$

where A_{dust} is the surface area concentration of aerosol mineral dust, F_{Kfsp} is the fraction of mineral dust composed of K-feldspar, $n_s(T)$ is the temperature-dependent ice-nucleating active site density for K-feldspar, T is temperature in °C, and $T_{\max}$ is the upper temperature limit of the fit. The first term represents the low-temperature part of the INP spectrum associated with mineral-dust-controlled nucleation, while the second term represents the strong curvature at warmer temperatures. For the median fit, $A_{\mathrm{dust}} = 4.94{\times}10^{-5}\,\mathrm{cm}^2\,\mathrm{L}^{-1}$, $F_{\mathrm{Kfsp}} = 0.05$, $T_{\max} = -4\,^{\circ}\mathrm{C}$, $a = 1.93{\times}10^{-22}\,\mathrm{L}^{-1}$, $b = 45.25\,^{\circ}\mathrm{C}^{-1}$, and $c = 0.046$.

We also include a comparison of the temperature dependence of the INP parametrisations of DeMott et al. (2010) and Daily et al. (2025) in Fig. S1.

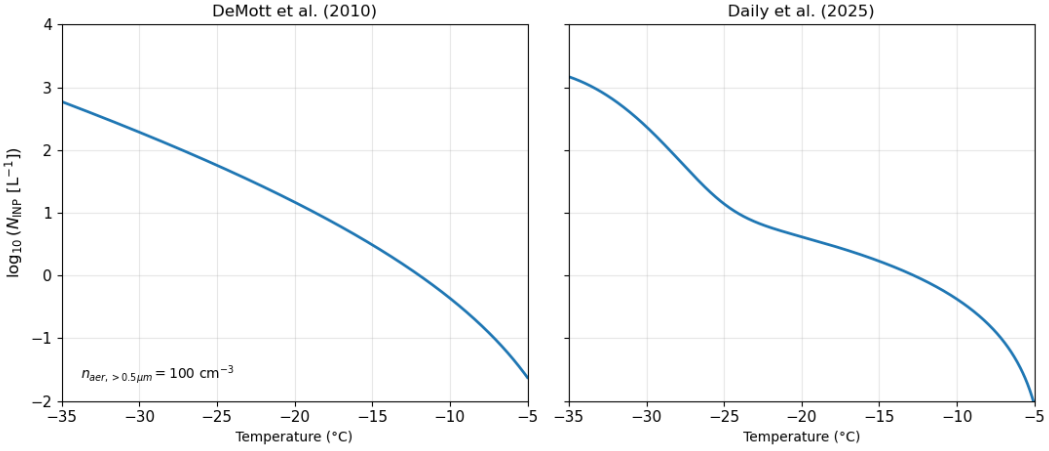

Figure S1. Comparison of the temperature dependence of the INP parametrisations of DeMott et al. (2010) and Daily et al. (2025). The figure shows $\log_{10}(N_{\mathrm{INP}})$ as a function of temperature for the two parametrisations using identical axes. For the DeMott et al. (2010) parametrisation, the aerosol number concentration for particles with diameters larger than $0.5\,\mu\mathrm{m}$ is fixed at $100\ \mathrm{cm}^{-3}$.

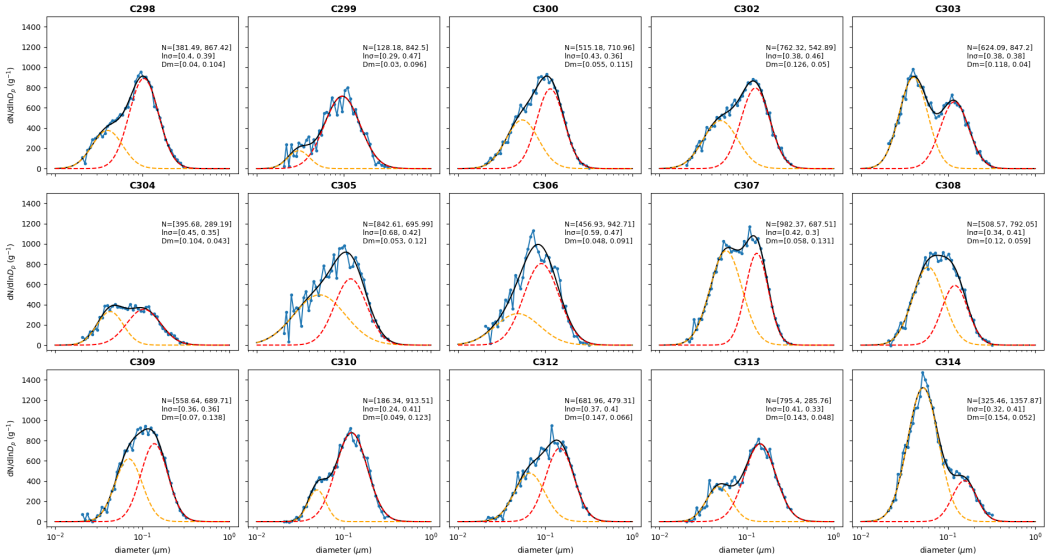

Figure S2. Aerosol particle size distributions measured by the SMPS for 15 flight cases (C298–C314) during the DCMEX campaign, together with two-mode lognormal fits. Blue lines represent observed size distributions, dashed lines indicate individual lognormal modes, and black lines show the total fit. Fitted parameters (number concentration, geometric standard deviation, and mean diameter) are shown in each panel.

Table S2. Summary of the two-mode lognormal fits to the SMPS aerosol measurements, providing the number concentration (N, cm^{-3}), mean diameter (D_{m}, nm), and geometric standard deviation ($\ln\sigma$, dimensionless) for Mode A and Mode B.

Date	Flight	Mode A			Mode B		
		N_A	D_{mA}	$\ln\sigma_A$	N_B	D_{mB}	$\ln\sigma_B$
Tue 19 Jul	C298	381.49	40	0.40	867.42	104	0.39
Wed 20 Jul	C299	192.27	30	0.29	1263.75	96	0.47
Fri 22 Jul	C300	515.18	55	0.43	710.96	115	0.36
Sun 24 Jul	C302	542.89	50	0.46	762.32	126	0.38
Mon 25 Jul	C303	847.20	40	0.38	624.09	118	0.38
Tue 26 Jul	C304	289.19	43	0.35	395.68	104	0.45
Wed 27 Jul	C305	842.61	53	0.68	695.99	120	0.42
Fri 29 Jul	C306	456.93	48	0.59	942.71	91	0.47
Sat 30 Jul	C307	982.37	58	0.42	687.51	131	0.30
Sun 31 Jul	C308	792.05	59	0.41	508.57	120	0.34
Mon 1 Aug	C309	558.68	70	0.36	689.68	138	0.36
Tue 2 Aug	C310	186.34	49	0.24	913.51	123	0.41
Thu 4 Aug	C312	479.31	66	0.40	681.96	147	0.37
Sat 6 Aug	C313	285.76	48	0.33	795.40	143	0.41
Sun 7 Aug	C314	1357.87	52	0.41	325.46	154	0.32

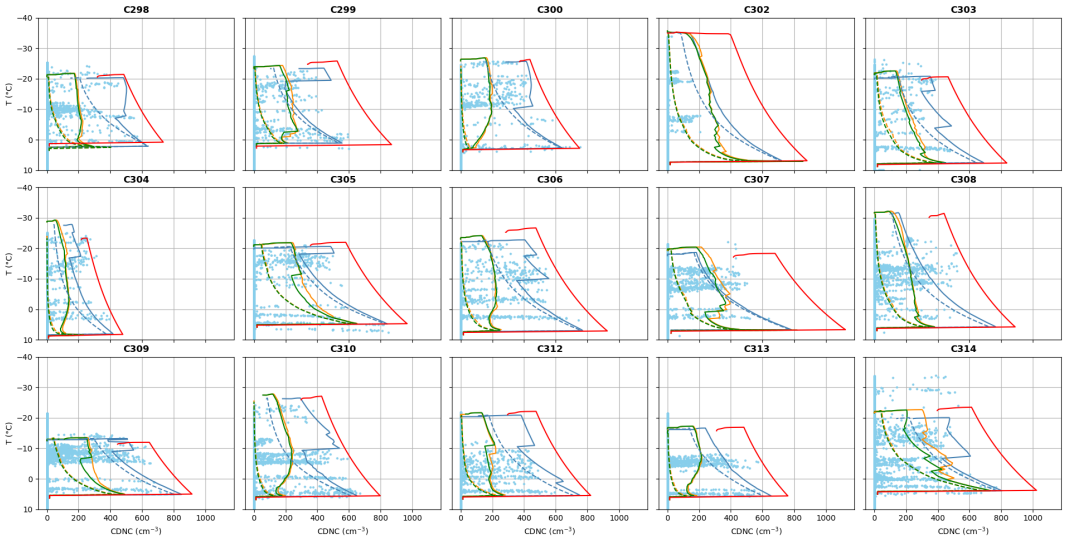

Figure S3. Vertical profiles of cloud droplet number concentration (CDNC) as a function of temperature for 15 flight cases (C298–C314) during the DCMEX campaign. Blue dots indicate observations; red lines denote ADIA; solid blue lines HOM+EA; dashed blue lines HOM; solid orange lines INHOM+EA+RA; dashed orange lines INHOM+RA; solid green lines INHOM+EA; and dashed green lines INHOM.

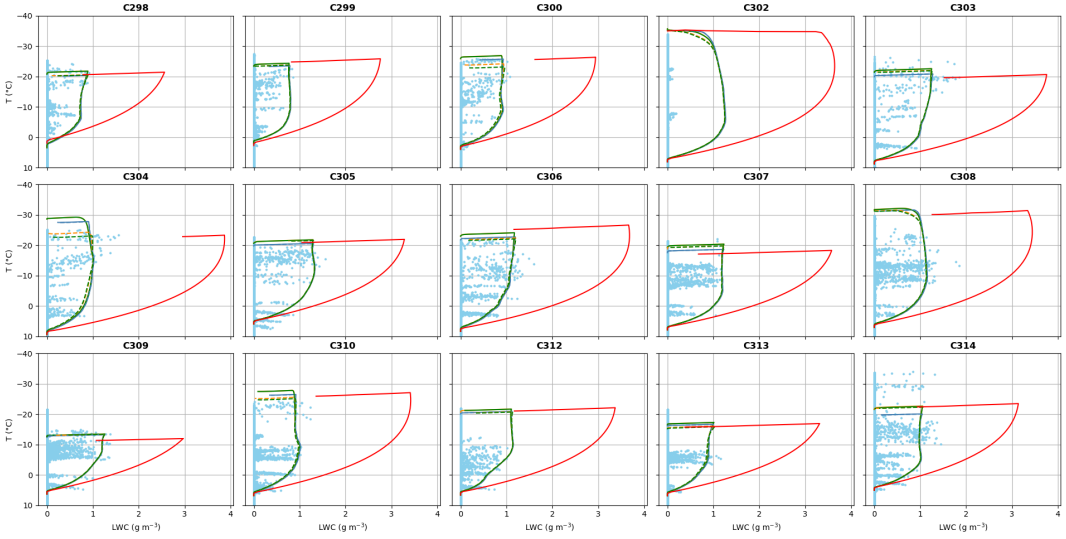

Figure S4. Vertical profiles of liquid water content (LWC) as a function of temperature for 15 flight cases (C298–C314) during the DCMEX campaign. Blue dots indicate observations, and coloured lines represent parcel model simulations (colour coding follows Fig. S3).

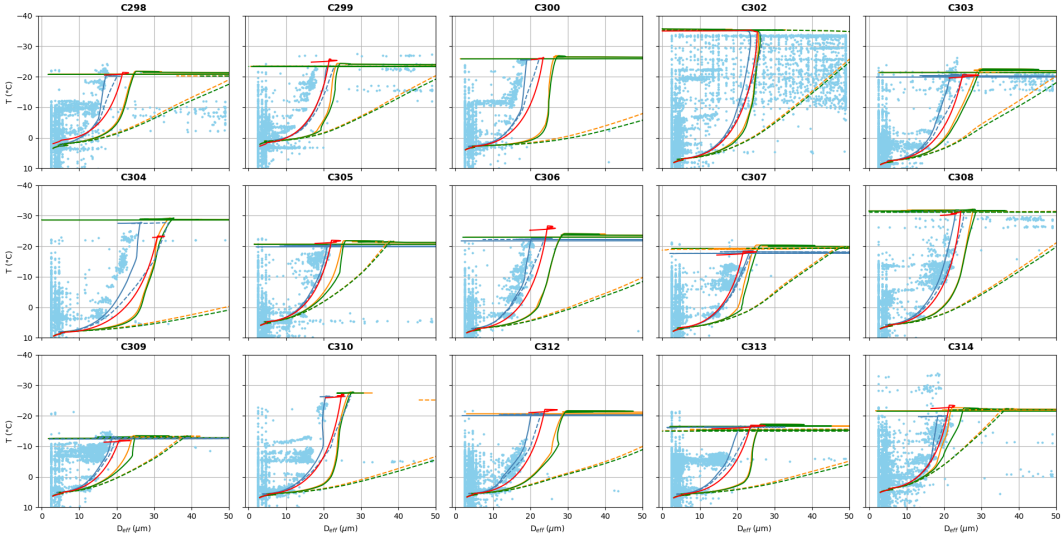

Figure S5. Vertical profiles of cloud droplet effective diameter (D_{eff}) as a function of temperature for 15 flight cases (C298–C314) during the DCMEX campaign. Blue dots indicate observations, and coloured lines represent parcel model simulations (colour coding follows Fig. S3).

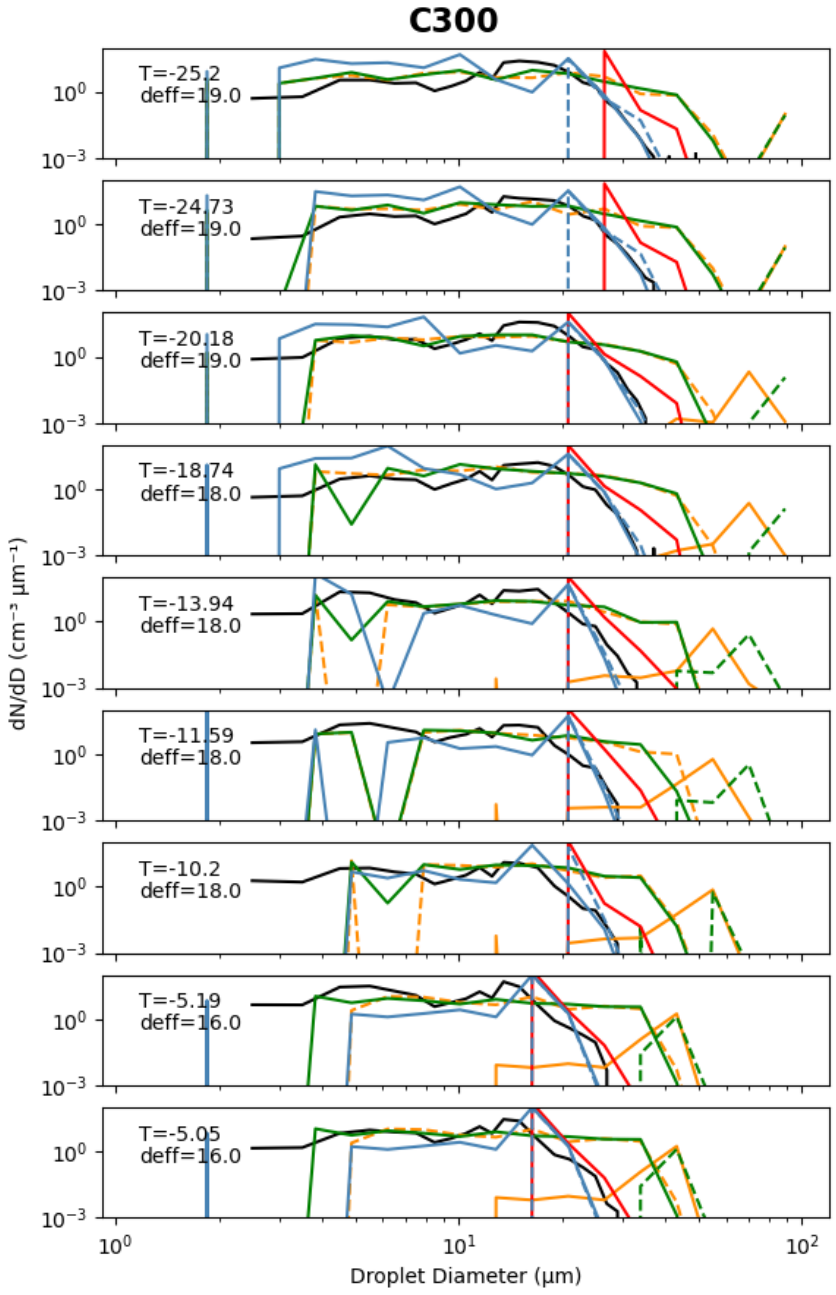

Figure S6. Droplet size distributions for the 22 July 2022 case at nine selected temperature levels. The black lines show the observations, while the coloured lines show the parcel model simulations (colour coding follows Fig. S3).

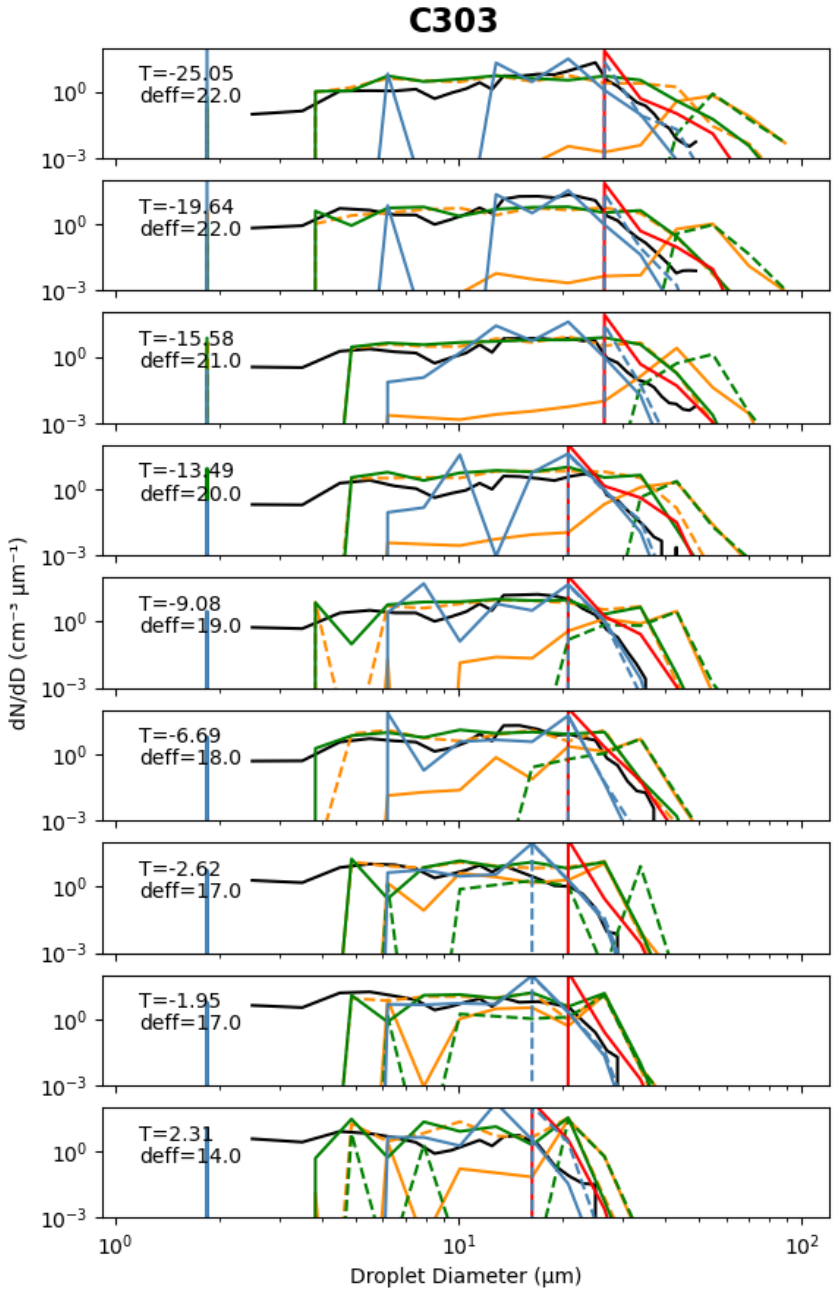

Figure S7. Droplet size distributions for the 25 July 2022 case at nine selected temperature levels. The black lines show the observations, while the coloured lines show the parcel model simulations (colour coding follows Fig. S3).

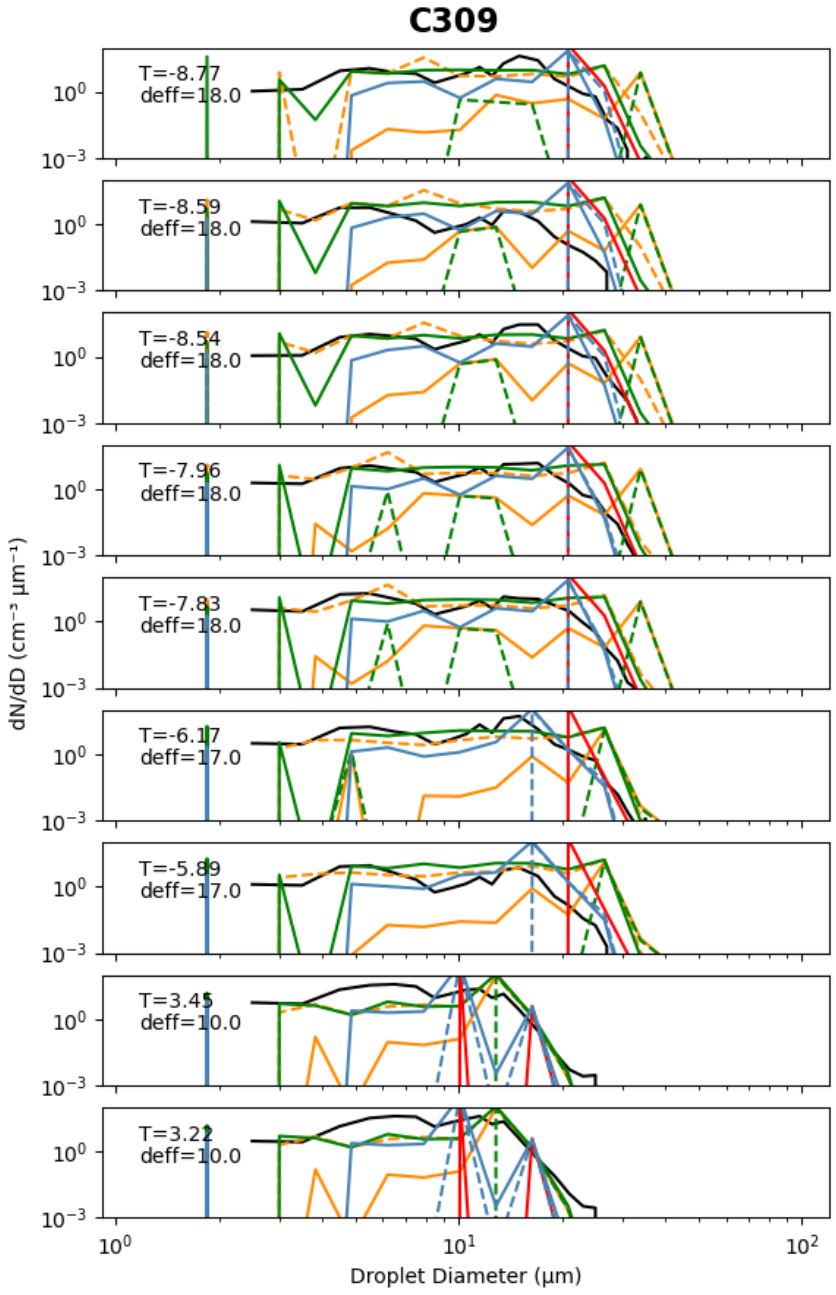

Figure S8. Droplet size distributions for the 01 August 2022 case at nine selected temperature levels. The black lines show the observations, while the coloured lines show the parcel model simulations (colour coding follows Fig. S3).

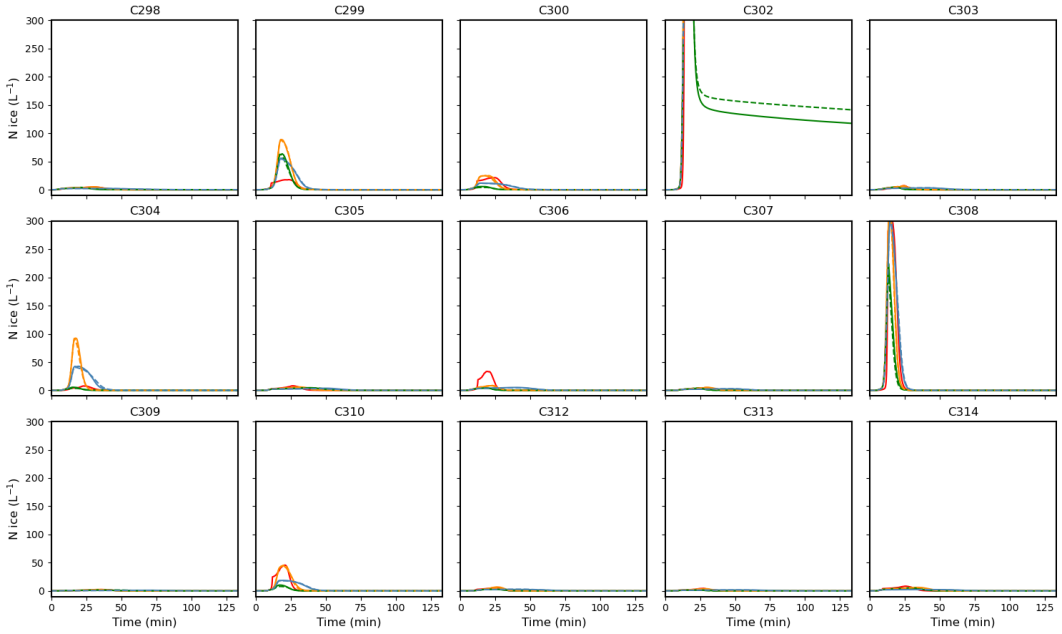

Figure S9. Time series of ice crystal number concentration (N_{ice}) for the 15 simulated flight cases (C298–C314) during the DCMEX campaign. All SIP mechanisms are switched off, and coloured lines represent parcel model simulations (colour coding follows Fig. S3).

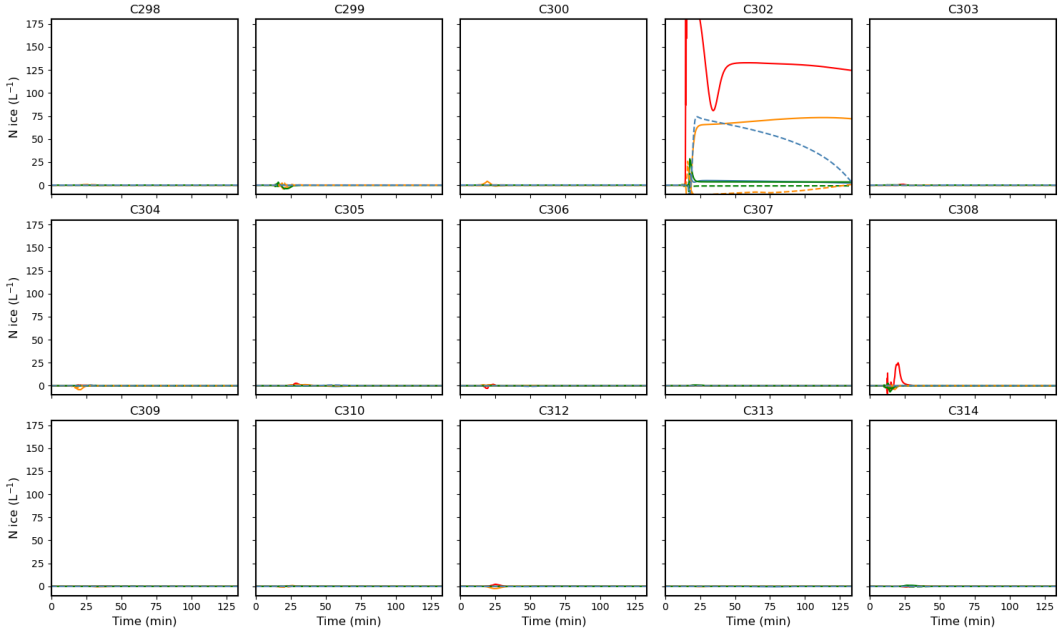

Figure S10. Ice enhancement for the 15 simulated flight cases (C298–C314) during the DCMEX campaign. Only RS is activated, and coloured lines represent parcel model simulations (colour coding follows Fig. S3).

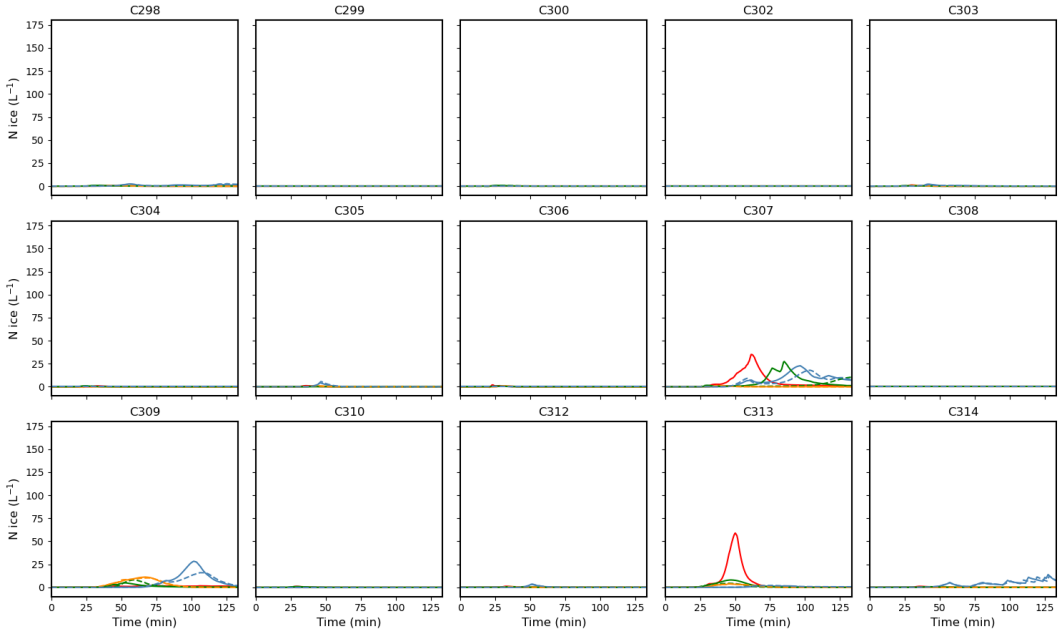

Figure S11. Ice enhancement for the 15 simulated flight cases (C298–C314) during the DCMEX campaign. Only CB is activated, and coloured lines represent parcel model simulations (colour coding follows Fig. S3).

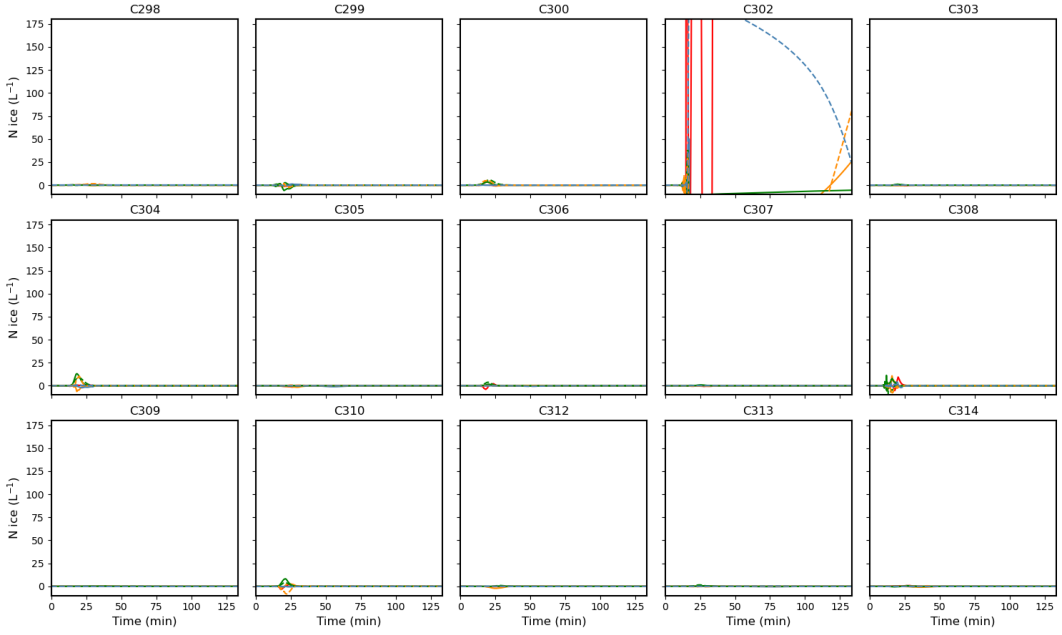

Figure S12. Ice enhancement for the 15 simulated flight cases (C298–C314) during the DCMEX campaign. Only M1 is activated, and coloured lines represent parcel model simulations (colour coding follows Fig. S3).

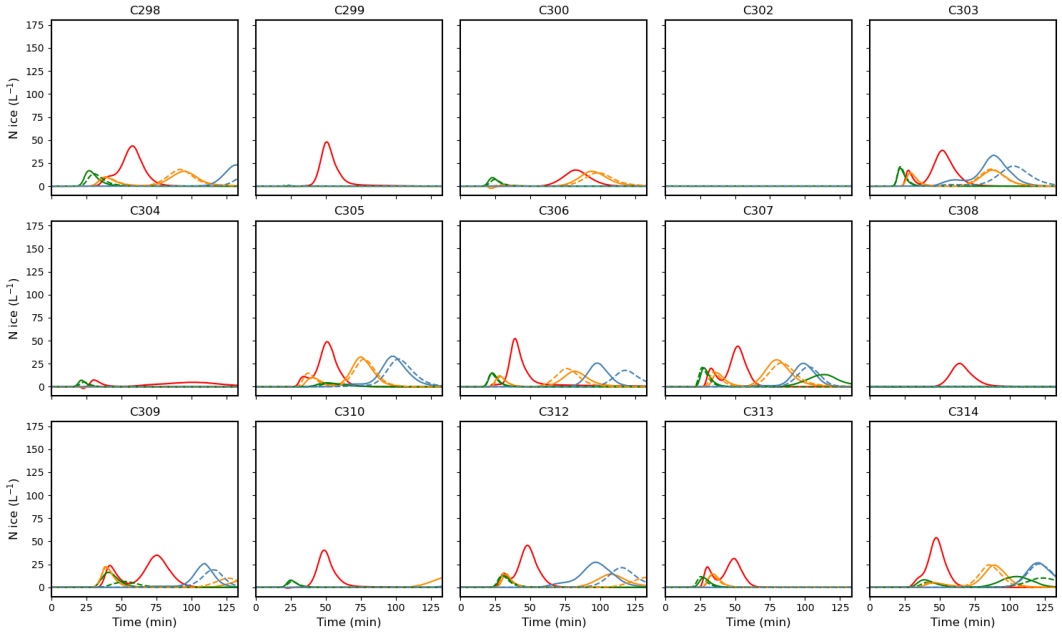

Figure S13. Ice enhancement for the 15 simulated flight cases (C298–C314) during the DCMEX campaign. Only M2 is activated, and coloured lines represent parcel model simulations (colour coding follows Fig. S3).

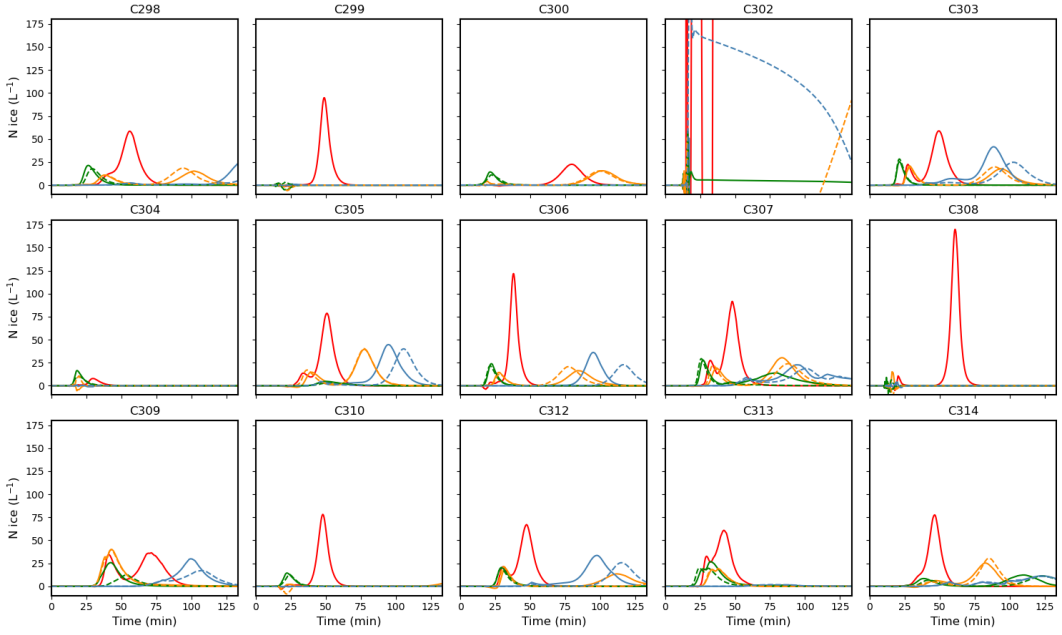

Figure S14. Ice enhancement for the 15 simulated flight cases (C298–C314) during the DCMEX campaign. All SIP mechanisms are activated together, and coloured lines represent parcel model simulations (colour coding follows Fig. S3).

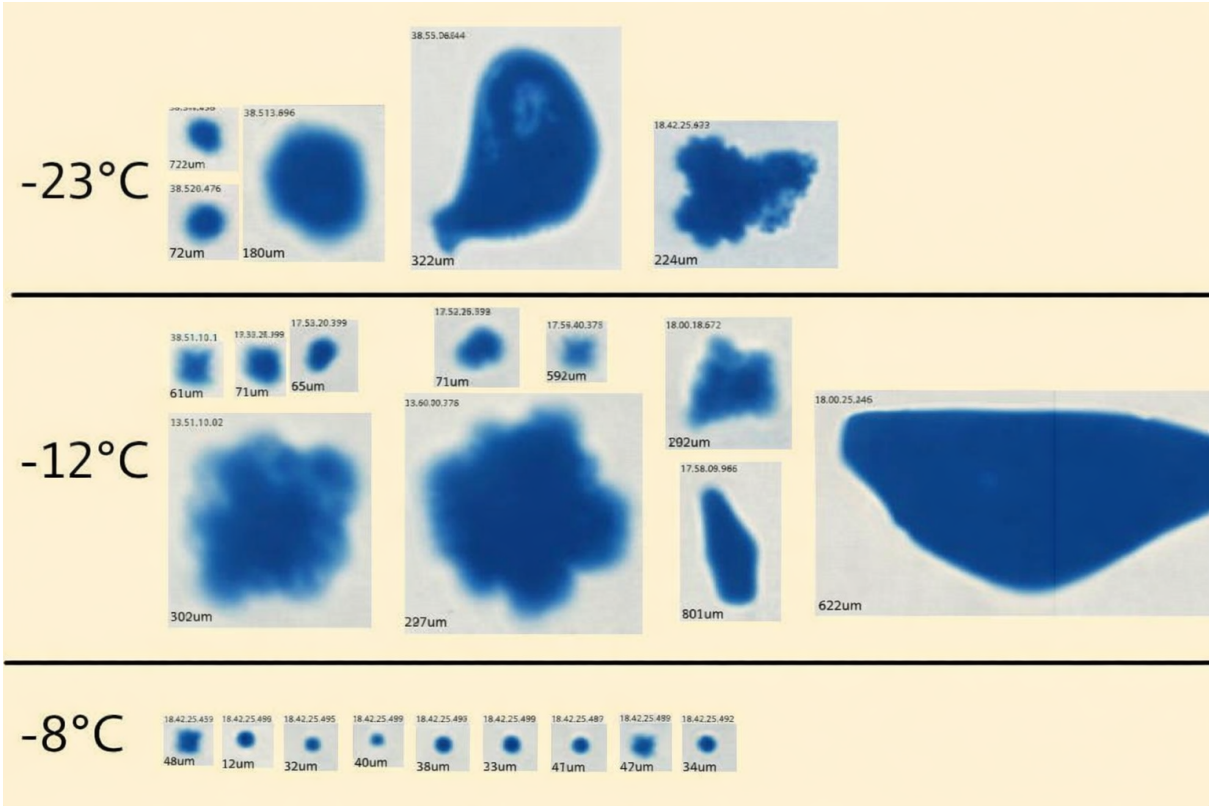

Figure S15. Observed CPI images of ice particles for the 22 July 2022 case at three selected temperature levels.

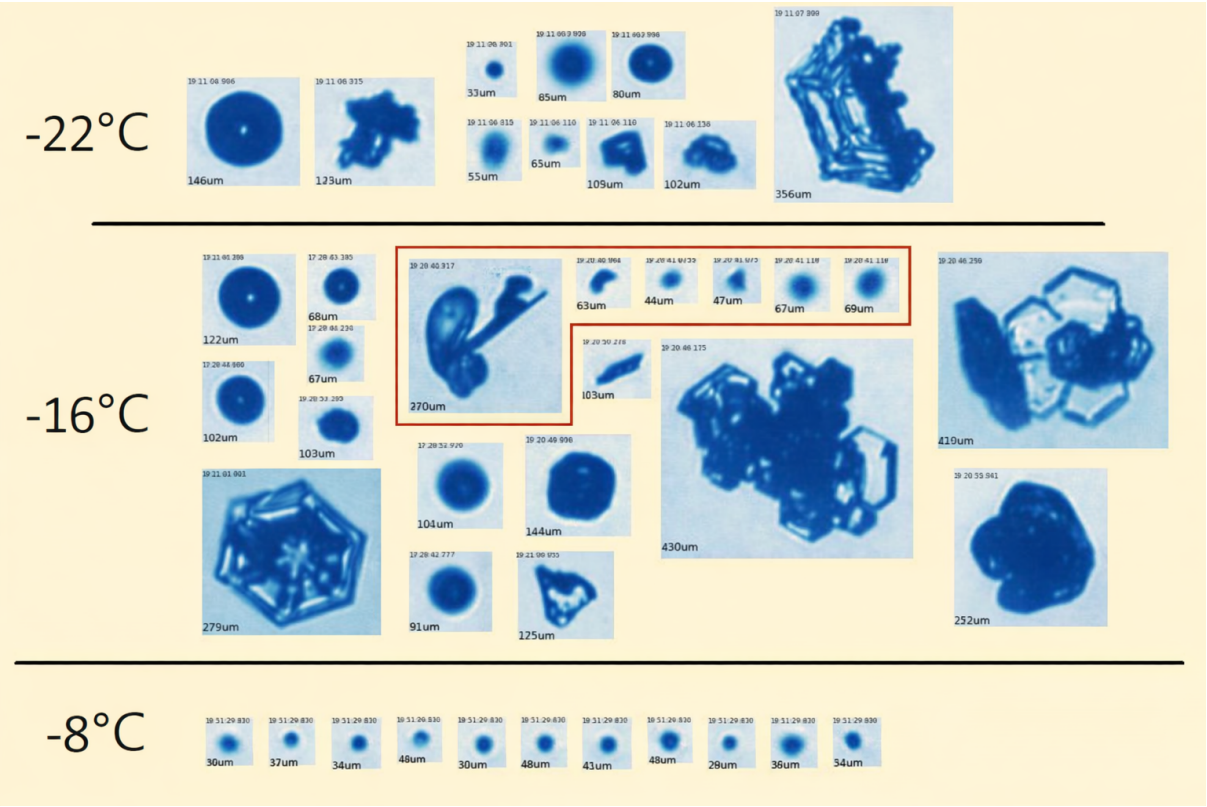

Figure S16. Observed CPI images of ice particles for the 25 July 2022 case at three selected temperature levels.

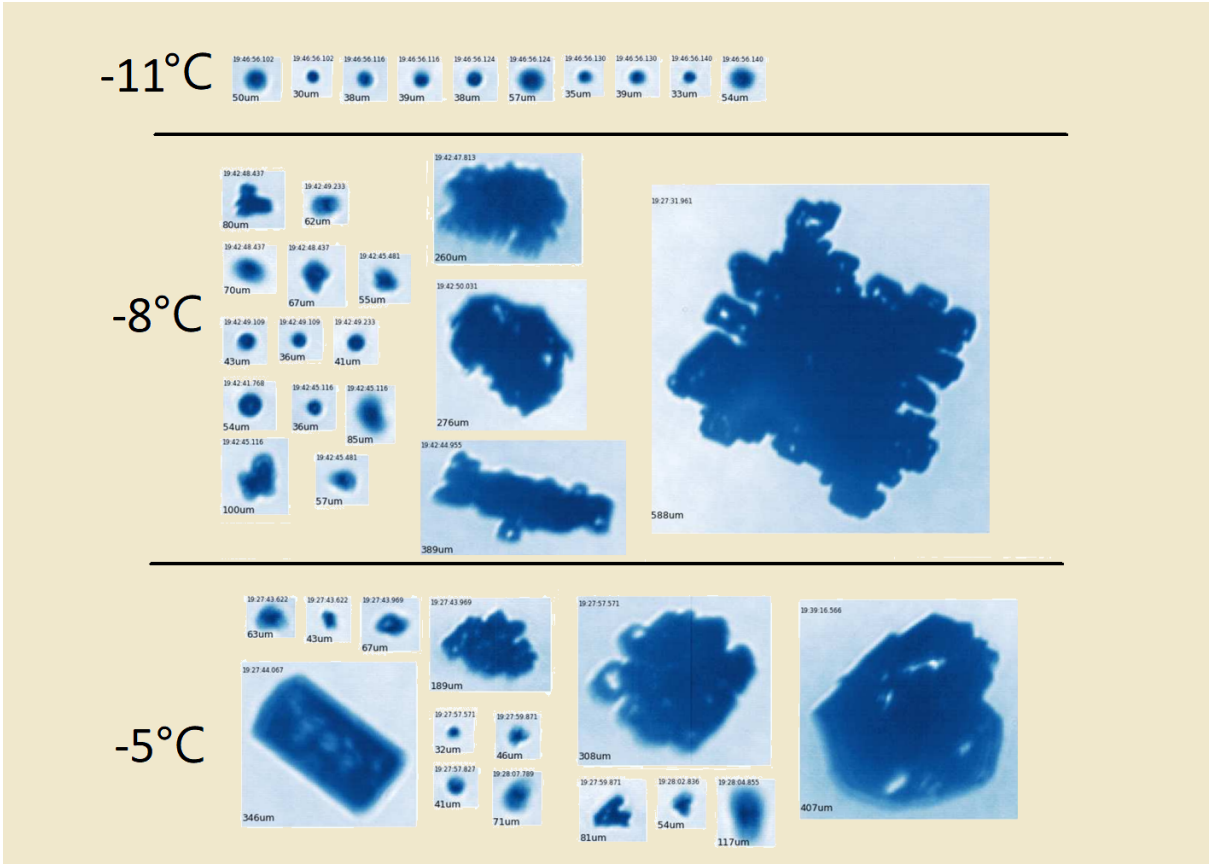

Figure S17. Observed CPI images of ice particles for the 01 August 2022 case at three selected temperature levels.

References

Bott, A.: A flux method for the numerical solution of the stochastic collection equation, J. Atmos. Sci., 55, 2284–2293, 1998.

Daily, M. I., Robinson, J., Finney, D. L., Raif, E. N., McQuaid, J. B., Sánchez-Marroquín, A., Hu, K., Lloyd, G., Flynn, M., Field, P. R., et al.: Ice-nucleating particle and cloud ice crystal concentrations associated with developing summertime deep convective clouds in south-western USA, Authorea Preprints, 2025.

DeMott, P. J., Prenni, A. J., Liu, X., Kreidenweis, S. M., Petters, M. D., Twohy, C. H., Richardson, M. S., Eidhammer, T., and Rogers, D. C.: Predicting global atmospheric ice nuclei distributions and their impacts on climate, Proc. Natl. Acad. Sci. U.S.A., 107, 11 217–11 222, https://doi.org/10.1073/pnas.0910818107, 2010.

Hallett, J. and Mossop, S. C.: Production of secondary ice particles during the riming process, Nature, 249, 26–28, https://doi.org/10.1038/249026a0, 1974.

James, R. L., Phillips, V. T. J., and Connolly, P. J.: Secondary ice production during the break-up of freezing water drops on impact with ice particles, Atmos. Chem. Phys., 21, 18 519–18 530, https://doi.org/10.5194/acp-21-18519-2021, 2021.

James, R. L., Crosier, J., and Connolly, P. J.: A bin microphysics parcel model investigation of secondary ice formation in an idealised shallow convective cloud, Atmospheric Chemistry and Physics, 23, 9099–9121, https://doi.org/10.5194/acp-23-9099-2023, 2023.

Phillips, V. T., Patade, S., Gutierrez, J., and Bansemer, A.: Secondary Ice Production by Fragmentation of Freezing Drops: Formulation and Theory, J. Atmos. Sci., 76, 3031–3070, https://doi.org/10.1175/JAS-D-17-0190.1, 2018.

Phillips, V. T. J., Yano, J.-I., and Khain, A.: Ice Multiplication by Breakup in Ice–Ice Collisions. Part I: Theoretical Formulation, J. Atmos. Sci., 74, 1705 – 1719, https://doi.org/10.1175/JAS-D-16-0224.1, 2017.

Reisner, J., Rasmussen, R. M., and Bruintjes, R. T.: Explicit forecasting of supercooled liquid water in winter storms using the MM5 mesoscale model, Q. J. R. Meteorol. Soc., 124, 1071–1107, https://doi.org/https://doi.org/10.1002/qj.49712454804, 1998.